Inverse Temperature Transition of a Biomimetic Elastin Model: Reactive Flux Analysis of Folding/Unfolding and Its Coupling to Solvent Dielectric Relaxation[†]

Marcel Baer,*,‡ Eduard Schreiner,‡ Axel Kohlmeyer,‡ Roger Rousseau,*,§ and Dominik Marx‡

Lehrstuhl für Theoretische Chemie, Ruhr-Universität Bochum, 44780 Bochum, Germany, and International School for Advanced Studies, Via Beirut 4, 34014, Trieste, Italy

Received: August 25, 2005; In Final Form: December 12, 2005

The inverse temperature transition (ITT) of a biomimetic model for elastin, capped GVG(VPGVG) in liquid water, is investigated by a comprehensive classical molecular dynamics study. The temperature dependence of the solvation structure and dynamics of the octapeptide are compared using three common force fields, CHARMM, GROMOS, and OPLS. While these force fields differ in quantitative detail, they all predict this octapeptide to undergo a "folding transition" to closed conformations upon heating and a subsequent "unfolding transition" to open conformations at still higher temperatures, thus reproducing the ITT scenario. The peptide kinetics is analyzed within the reactive flux formalism applied to the largest-amplitude mode extracted from principal component analysis, and the solvent's dielectric fluctuations are obtained from the total water dipole autocorrelations. Most importantly, preliminary evidence for an intimate coupling of peptide folding/unfolding dynamics, and thus the ITT, and dielectric relaxation of *bulk water* is given, possibly being consistent with a "slave mode" picture.

1. Introduction

Elastic fibers as found in skin, lungs, and vascular walls of vertebrates consist of fibrilous components, fibrilin and collagen, and a globular component, elastin,[1] of which the latter is providing the elasticity.[2–7] Elastin is an extensively cross-linked polymer of tropoelastin and exhibits remarkable elastic properties in the water-swollen state. Tropoelastin itself is composed of a lysine-rich domain where the fibers can be cross-linked and a second domain composed largely of nonpolar residues with a highly repetitive pentameric unit, VPGVG (amino acids, V, valine; P, proline; and G, glycine). Detailed investigation revealed that this fundamental pentameric unit is at the core of elastin's intriguing mechanical properties.[8,9] Hence biopolymeric elastin mimetic materials based on repetition of the fundamental VPGVG unit have been designed and extensively studied for their mechanical properties with the promise of potential use in biomechanical devices.[6,7,10,11] Despite the intense interest in these materials the solution-phase structure of elastin and its mimics has proven to be highly elusive, and hence the molecular level understanding of the origin of its viscoelastic properties remains inconclusive.

One of the many fascinating properties of elastin-like materials is that they undergo a so-called "inverse temperature transition" (ITT), a process whereby the molecule changes from an extended ("disordered" or "unfolded") conformation to a compact ("ordered" or "folded") one upon *heating* to a temperature typically above 25 °C.[4,6,12–14] In this state, elastin provides elasticity variously ascribed to classical rubber elasticity,[15] one of several librational entropy mechanisms,[3,8,16] multiphase models[2] and hydrophobic hydration.[14] Beyond doubt, however, is the critical role played by water as a plasticizer,

since dry elastin is brittle.[17] Nuclear magnetic resonance studies on both water-swollen elastin and solvated elastin mimetic polymers find that the peptide consists of highly mobile chains.[18–23] Circular dichroism (CD), Fourier transform infrared, and Raman spectroscopical studies on elastin-like polypeptides suggest the presence of β- and γ-turns that may be in dynamic equilibrium.[9,24–27] Recent NMR studies suggest that poly-(VPGVG) exhibits multiple states as a function of temperature characterized by different peptide dynamics and peptide–water interactions.[23,28]

In contrast to the wealth of experimental data available on these materials there are far fewer theoretical studies. The elastic properties of a model peptide under external constraints, to mimic an atomic force microscopy pulling experiment, have been studied using relatively short molecular dynamics (MD) simulations.[14,16] The earliest of these studies underscored the importance of librational entropy[16] in determining the elastic properties of these materials, whereas the later[14] studies have stressed the critical role played by the solvating water molecules. In addition, the ITT has been studied by MD on a solvated 90 amino acid polypeptide as a function of temperature.[29,30] These latter simulations have had great success in qualitatively explaining many of the experimental observations based upon an analysis of thermodynamic and average structural parameters. We note, however, that the simulations performed so far were based on relatively short simulation times of at most a few nanoseconds. This is not sufficient to *quantitatively* converge either average or dynamical quantities for such large systems, in particular in view of the time scale of the peptide's intrinsic conformational relaxation.[23]

Following the experimental observation of Reiersen et al.[9] that the ITT may be observed in oligopeptides as small as eight amino acids, in particular GVG(VPGVG), the current researchers have performed 32 ns MD simulations at 12 temperatures on this octapeptide to analyze the ITT in this system.[25,31] The primary result of this study was that the octapeptide behaved

ITT of a Biomimetic Elastin Model

J. Phys. Chem. B, Vol. 110, No. 8, 2006 **3577**

like a two-state system that was characterized as consisting of both extended and folded structures. The ITT was characterized by a variation in the relative populations of each type of structure with transitions between the minima governed by a single large-amplitude mode with correlation times on the order of a few hundred picoseconds. Most interesting was the realization that the peptide motions and the peptide−water interactions were intimately interconnected, leading to a reciprocity between the nanosecond time scale fluctuations of the peptide backbone and the picosecond time scale fluctuations of the interfacial hydrogen bonds (HBs), i.e., those between the peptide and the first-shell solvation water, both of which were crucial factors leading to the ITT. However, as with most classical MD studies, it is not clear to what degree the observed microscopic details result from the particulars of the simulation such as the biomolecular force field (CHARMM), external control parameters (constant temperature), boundary conditions (droplet stochastic), and trajectory lengths (32 ns) employed. Most importantly, the very relationship between peptide conformational dynamics and the solvent's microscopic fluctuations needs further clarification in view of the uncovered coupling. This computational observation[25,31] may have specific relevance to the recent experimental finding that peptide motions may be intrinsic to the peptide structure but also may be so-called "slave modes" in that they are dictated by the solvent fluctuations.[32]

To address these issues a first simple but nevertheless fundamental ingredient is longer simulation times. This is true from the perspective of improved statistical convergence for obtaining both thermodynamical quantities as well as dynamical and kinetic insights into the details of this process, the ITT. Although the former objective may be appropriately addressed by employing free energy based enhanced sampling methods,[33−35] the discovered dynamical relationship between the peptide−water interactions and peptide motion itself necessitates long and continuous dynamics trajectories. Since the primary interest here is the dynamics and kinetics of the peptide coupled to solvent fluctuations, we cannot make use of techniques such as the replica exchange method, which improves conformational sampling at the expense of destroying the dynamical information. Coarse-grained force field models, as recently developed by Klein and co-workers,[36,37] are better suited to sampling the peptide dynamics as such, especially for even larger elastin models, but the role of the picosecond fluctuations of the solvating water molecules and their coupling to the ITT of the peptide needs to be clarified further at the atomistic resolution level. Finally, since the time scale and atomistic details of the ITT will depend on the peptide force field (and the associated water potential against which it has been parametrized) a comprehensive understanding of this process should be addressed for a wide class of force fields to determine the relevant features that are *not* dependent upon the particular potential employed.

To further the understanding of the nature of the ITT in elastin-like peptides we perform detailed simulations in the isobaric−isothermal ensemble for a solvated octapeptide, Ac-GVG(VPGVG)-Me, based on trajectories in the range of 60 to 140 ns and 10 temperatures between 300 and 420 K. Our first goal is to compare and to contrast the results of the simulations for three distinct biomolecule/water potential functions, CHARMM/TIPS3P, GROMOS/SPC, and OPLS/TIP3P, and to provide a broader basis for extracting further insights into the "universal" microscopic details of the system. In addition to standard analysis such as principal component analysis, the peptide kinetics will be cast into the language of a reactive flux

formalism, and the solvent's dielectric relaxation properties are investigated with respect to possible couplings to the peptide dynamics.

2. Computational Methods

To obtain quantifiable results, considerable effort and care have been spent on setting up and performing a comparative series of simulations of the solvated model peptide. In total, about 4 μs worth of simulation time, in addition to substantial equilibration runs for each temperature and force field, was used for analysis. In the following, we describe in detail the specific choices of parameters employed for the various force fields, water potentials, and the respectively used simulation codes. This technical part closes with an outline of the methods used for the data analysis.

2.1. General Setup and Preparation. Three series of classical molecular dynamics simulations were performed at 10 temperatures (300, 310, 320, 330, 340, 350, 360, 380, 400, and 420 K) using the CHARMM-22,[38] GROMOS-43a1,[39] and OPLS-AA/L[40] force fields. These three force fields are known[41−43] to have different characteristics in terms of stabilizing different structural motifs of peptides. There is evidence, at least for purely hydrophobic interactions, that also the choice of water potential has an impact on the accurate description of the hydration.[44] However, since peptide force fields are parametrized with respect to a specific water model, it is crucial for our investigation to employ them consistently to preserve the delicate balance of the interactions between peptide and solvent. Thus, each force field has been used with its *matching* water potential, that is TIPS3P,[47] SPC,[45] and TIP3P,[46] respectively. For simplicity we will label the three setups with CHARMM, GROMOS, and OPLS for the remaining part of the paper; references to a previous study[25,31] will be labeled with EGO.[48]

In all cases the system consists of an eight amino acid oligopeptide with the sequence GVG(VPGVG) capped by methylamine ($-NH-CH_3$) and acetyl ($-COCH_3$) groups at its C- and N-terminus, respectively, that is Ac-GVG(VPGVG)-Me. The peptide is solvated with explicit water in a cubic unit cell subject to periodic boundary conditions in the isobaric−isothermal ensemble; see below for details used to impose pressure and temperature control.

To ease the equilibration process, especially at the lower temperatures, a particular configuration from the previous EGO simulation study was chosen as the starting configuration; see Figure 1. The selected configuration, including the surrounding water molecules, was taken from the final part of the 290 K EGO trajectory and chosen for being particularly extended. The peptide plus surrounding water was then inserted into a cubic box of preequilibrated water with about 5 Å distance between the walls and the inserted water block, thus ensuring a large enough distance between the periodic images of the peptide to be able to disregard self-interactions. The system was then equilibrated in the isobaric−isothermal ensemble at the required target temperatures and at 1 bar external pressure, while initally keeping the preequilibrated molecules fixed and then gradually releasing the outmost water molecules followed by the inner molecules and finally the peptide. For *each* trajectory the system was further equilibrated under the final conditions for another 6 ns in the cases of the GROMOS and OPLS simulations and for 3 ns in case of the CHARMM simulations. Equilibrated configurations were collected every picosecond for 100, 60, and 140 ns for the CHARMM, GROMOS, and OPLS simulations, respectively. The resulting averaged densities for SPC and TIP3P water far away from the peptide matched the published bulk water density versus temperature data.[44]

2.2. GROMOS/SPC Simulation Parameters. The first set of trajectories was using the GROMOS-43a1 united atom force field[39] as implemented in the Gromacs simulation package,[49,50] version 3.1, using 4362 SPC[45] water molecules. The equations of motion were integrated using the leapfrog[51] version of the Verlet algorithm at a time step of 1 fs. All peptide hydrogen bonds were constrained using the LINCS[52] algorithm, and the water molecules were kept rigid using the SETTLE[53] formulation of the SHAKE[54] algorithm for water molecules.

To establish the isobaric−isothermal ensemble a Nosé−Hoover[55,56] thermostat (characteristic time, $\tau = 0.25$ ps) was used in combination with a Parrinello−Rahman barostat algorithm[57,58] (characteristic time, $\tau = 0.5$ ps, reference pressure, 1 bar, compressibility 4.5×10^{-5} bar^{-1}). Lennard-Jones interactions were cut off at 12 Å, whereas Coulomb interactions were handled using a particle mesh Ewald summation[59] with a Fourier grid spacing of 0.12 nm, fourth-order interpolation, and a real-space cutoff of 12 Å. At 300 K the average edge length of the simulation cell was 51.4 Å, and the maximal extension of the peptide was 26.8 Å, leaving a worst case distance of almost 25 Å between the periodic images of the peptide.

2.3. OPLS/TIP3P Simulation Parameters. The second series of trajectories used the OPLS-AA/L[40,60] all-atom force field, again as implemented in the Gromacs simulation package;[49,50] thus identical simulation parameters, cutoffs and boundary conditions, and number of solvating water molecules were chosen. However, for consistency with the force field parametrization, the TIP3P[46] water potential was chosen over the SPC model. At 300 K the average edge length of the simulation cell was 51.2 Å, and the maximal extension of the peptide was 29.2 Å, leaving a worst case distance of over 20 Å between the periodic images of the peptide.

2.4. CHARMM/TIPS3P Simulation Parameters. For the third set of simulations the CHARMM-22[38] all-atom force field was employed. In this case, however, the NAMD[61] simulation package, version 2.5, was used. The equations of motion were integrated using the velocity Verlet algorithm with a time step of 1 fs. All peptide hydrogen bonds and the water molecule geometry were constrained using RATTLE[62] of the SHAKE[54] algorithm. Like beforehand, Lennard-Jones interactions were cut off at 12 Å, and Coulomb interactions were handled using a particle mesh Ewald summation[59,63] with fourth-order interpolation, and a real-space switching function between 12 and 14 Å was used. In this case, a Langevin piston barostat/thermostat combination[64,65] had to be employed to control pressure and temperature.

Again the consistent water potential, TIPS3P,[47] was employed. The TIPS3P potential is a modified version of the TIP3P potential with additional Lennard-Jones terms on the hydrogen atoms to offset the comparatively high partial charges on the peptide atoms in the CHARMM22 force field. The systems in this case contained only 3851 water molecules. At 300 K we found an average edge length of 48.6 Å. The maximal extension of the peptide during the course of the simulation was 30.1 Å, thus leaving a worst case distance of 18.5 Å between the peptide and its periodic images.

2.5. Data Analysis Methods. The total trajectory data of all simulations represent an accumulated simulation time of about 4 μs. Sampled at 1 ps distance and in single precision it consumes roughly 1 Terabyte of storage. Thus the data have to be reduced or preprocessed for most analysis steps. This was done using the VMD[66] package, which provides a versatile and simulation package independent scripting interface for manipulation of the data. Due to the large amount of data, time-consuming analysis steps were done as external programs with customized extensions.

End-to-End Distance. The distance $r_{cn}(t)$ between the C- and N-terminus is for this short polypeptide a convenient measure of its "size" or extension. Qualitatively, its behavior is very similar to that of the radius of gyration.

Principal Component Analysis. Briefly, in the covariance or principal component analysis (PCA)[67−70] approach one computes, by means of time averaging over the entire MD trajectory, the covariance matrix $\mathbf{C} = \langle [\mathbf{x}(t) - \langle \mathbf{x} \rangle] \cdot [\mathbf{x}(t) - \langle \mathbf{x} \rangle]^T \rangle$, where $\mathbf{x}(t) = \{\mathbf{x}_i(t)\}$ are the Cartesian coordinates of the peptide atoms at time t in a frame of reference where the overall translations and rotations of the polymer have been subtracted. The $3N - 6$ normalized eigenvectors $\{\mathbf{m}_i\}$ with nonzero eigenvalues $\{\lambda_i\}$ provide a basis in which the complex polypeptide motion may be decomposed. This allows us to disentangle relevant peptide backbone motions from small-amplitude vibrations via projection of the deviations of the MD trajectories from the average structure onto the eigenvectors, i.e., $m_i = [\mathbf{x}(t) - \langle \mathbf{x} \rangle] \cdot \mathbf{m}_i$. Ideally, for uncorrelated small-amplitude vibrations the corresponding projections m_i will simply fluctuate about an average value, yielding an approximately Gaussian distribution function, $P(m_i)$; the width might be temperature-dependent akin to harmonic molecular vibrations. Strong deviations from such a unimodal behavior would single out "interesting modes", that are possible order parameters or reaction coordinates, which can be associated to collective changes involving many atoms. When the temperature is changed the various modes are expected to mix, in particular the higher-order modes. Thus, a common basis $\{\tilde{\mathbf{m}}_i\}$ has to be chosen to ensure a consistent analysis. In the following, projections $\{\tilde{m}_i\}$ will be performed onto the basis of eigenmodes of the 300 K trajectory for each force field.

Reactive Flux Correlation Function Formalism. As described in subsection 3.2, we are actually able to obtain from the PCA an order parameter from the lowest eigenvector $\tilde{\mathbf{m}}_1$. Using the time dependence of its projection, $\tilde{m}_1(t)$, defined above, we evaluate the rate constants for folding, k'_f, and unfolding, k'_{uf}, by constructing a reactive flux time-correlation function as defined for a two-state system[71]

$$k_{f/uf}(t) = \frac{1}{x_{o/c}} \langle v(0) \delta(\tilde{m}_1(0) - \tilde{m}_1^{\ddagger}) H_{c/o}(t) \rangle$$

where $x_{o/c} = [o/c]/([c] + [o])$ with $[c/o]$ being the average concentration of open (unfolded)/closed (folded) species. The function $H_{c/o}(t)$ is 1 if the peptide is designated to be in a closed/open configuration and zero otherwise, with a dividing surface between the two states, i.e., a transition state, located at $\tilde{m}_1 = \tilde{m}_1^{\ddagger}$, and $v(t)$ is the velocity along the reaction coordinate. The functions $k_{f/uf}(t = 0)$ represent the transition state theory estimate of the rate constants, k'_{TST}, which amounts to assuming all trajectories that cross $\tilde{m}_1(t) = \tilde{m}_1^{\ddagger}$ remain in a given minimum, whereas the *real* rate constants, k', are obtained from a plateau behavior of $k_{f/uf}(t)$ for $t > \tau_p$, where τ_p is the internal relaxation time of the peptide. Hence, $k'_{f/uf}$ is extracted from an average over all trajectories that cross the transition state and remain there for a sufficient time. In general, all simulations here are of sufficient duration to provide several hundreds of significant crossing events; hence a well-defined plateau region for $k_{f/uf}(t > \tau_p)$ can be extracted, with the worst statistics occurring for the 300 K GROMOS simulation where only ∼100 crossings were obtained, so that all rate constants reported in subsection 3.3 were obtained without invoking transition state theory. The velocities were calculated by finite differences of projections
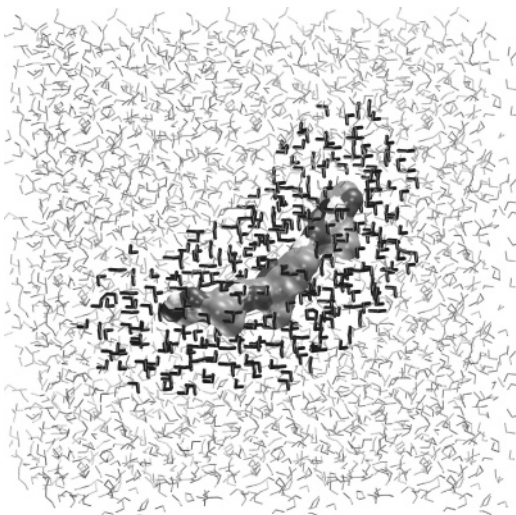
ITT of a Biomimetic Elastin Model

J. Phys. Chem. B, Vol. 110, No. 8, 2006 **3579**

Figure 1. Snapshot of the initial configuration used in all runs. The peptide and the water molecules marked in black were transferred from a previous study (EGO); see section 2.1.

$\tilde{m}_1$ as a function of time, and $\tilde{m}_1^{\ddagger}$ is extracted from the order parameter distribution function $P(\tilde{m}_1)$.

Solvent Dielectric Relaxation. Following previous publications[72,73] on the calculation of dielectric properties for peptide solutions in water, we calculated the total dielectric relaxation times from the autocorrelation function, $C_s(t) = \langle \mathbf{M}_s(0) \cdot \mathbf{M}_s(t) \rangle$, of the total dipole moment, $\mathbf{M}_s$, of *all water molecules* in the system. The short-time behavior of $C_s(t)$ did not match a single-exponential fit. Thus, to obtain the total dielectric relaxation time of the solvent, τ_{diel}, or correspondingly the dielectric relaxation rate, $k_{\text{diel}} = 1/\tau_{\text{diel}}$, the well-converged short- and intermediate-time part of $C_s(t)$ was integrated numerically and then completed by an extrapolation from a single-exponential fit to the well-converged data in the intermediate-time range. The intermediate-time data fit very well to a logarithmic form, and the extrapolation thus allows for a controllable source of error for the long-time decay of the function. We note in passing that the commonly used biexponential fit would not represent the short-time range data equally well for *all* temperatures and was found to have a greater dependence on the numerical noise in the nonconverged part of $C_s(t)$ and hence was not employed.

2.6. Convergence Checks and Error Bar Estimation. Crucial for the present simulation study is a sufficient sampling of the available phase space. To monitor how fast and how long novel peptide conformations are generated during a particular simulation, a classification scheme based on the dihedral angles (ψ, ϕ) about the peptide bonds is used.[74] To discretize the time series of these angles we define "by hand" the attractor basins for each angle based on its sampled probability density. For each angle clearly two structures can be identified and assigned to the symbols "a" or "b", which define for each conformation of the peptide a string of symbols. In Figure 2 the number of novel conformations (as indicated by the occurrence of a new string) that is generated as a function of time is plotted for the OPLS force field at low, intermediate, and high temperatures. The figure shows that after several tens of nanoseconds not many additional conformations, in the sense of the coarse-grained representation used, are added to the statistical sample indicated by the flattening of the running integrals. The ratios of the integrals in the ranges of 0−50 ns to 50−115 ns are 0.93 and 0.98 at 300 and 420 K, respectively. In addition, it can be seen that the sampling becomes more efficient at higher temperatures.
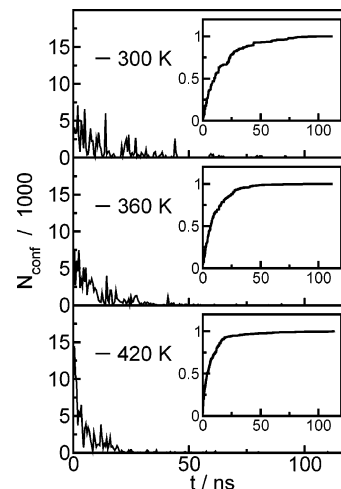

Figure 2. Number of novel conformations, N_{conf}, generated as a function of simulation time at the three indicated temperatures for the OPLS force field. The data are smoothened with a step window function of 0.5 ns width for the sake of presentation. The insets show the corresponding normalized running integrals.
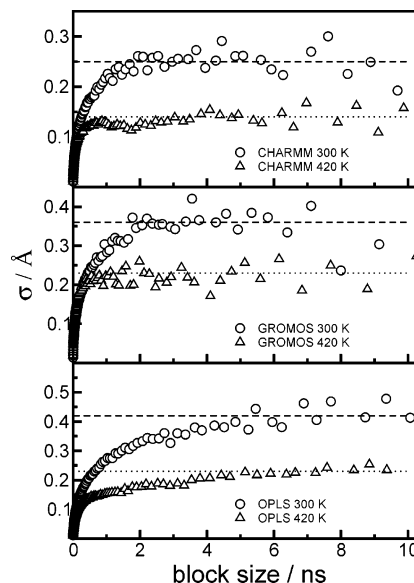

Figure 3. Block-averaged standard deviation, $\sigma(t)$, of the end-to-end distance, r_{cn}, as a function of block length t for low and high temperatures and the three free force fields used in this study. The horizontal lines mark the plateau values.

A reliable method to quantify statistical error bars is the block average or plateau analysis method.[75,76] The standard deviation of an observable of interest, $\sigma(t)$, is computed by dividing the available trajectory into nonoverlapping blocks of a given length t. Plotting σ versus t eventually leads to a constant plateau value for a range of intermediate block lengths, which is the statistical error bar. In Figure 3 this analysis is depicted for all three force fields at low and high temperatures using the end-to-end distance as observable; qualitatively similar behavior is obtained for other such observables. All functions $\sigma(t)$ feature extended plateau regions, which indicate statistical convergence in all cases.

Although the block average method is readily applied to structural quantities such as the end-to-end distance or various HB populations, it is less straightforward when it comes to more complex quantities such as reaction rates, $k_{\text{f/uf}}$, or equilibrium constants, K_{eq}. In these cases a much simpler approach is used whereby approximate error bars are estimated by performing the same analysis separately on the first and second halves of
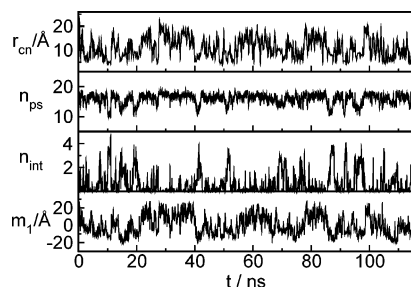
Figure 4. Selected structural quantities as a function of time for the OPLS force field at $T = 300$ K, from top to bottom: end-to-end distance, r_{cn}; number of peptide−solvent HBs, n_{ps}; number of peptide−peptide HBs, n_{int}; and projected largest-amplitude PCA eigenmode, $\tilde{m}_1$. See text for definitions.

Figure 5. Representative configurations for the OPLS force field at $T = 300$ K: (a) open conformation; (b) closed conformation. The open and the closed structures were obtained at times $t \approx 99$ ns and 20 ns, respectively, from the trajectories in Figure 4.

the trajectories. For structural quantities the two approaches are found to yield error bars of similar magnitude, indicating the usefulness of the second approach. Of course, the latter leads to larger uncertainties (i.e., error bars) of the computed error bars themselves.

3. Results and Discussion

To elucidate the ITT in the three commonly used force fields we have divided our discussion into three parts. For a first characterization of the transition we examine the structure of the solvated octapeptide as a function of temperature. In the second subsection we analyze dynamics via principal component analysis to obtain a meaningful order parameter. Finally, the peptide kinetics is investigated as well as the water dielectric relaxation with the aim to shed light on the possible coupling between peptide and solvent modes.

3.1. Structure and Hydrogen Bonding. To begin our discussion we consider the time evolution of a few selected structural parameters for the representative $T = 300$ K OPLS trajectory. Specifically the distance of the termini, r_{cn}, is considered as a simple measure of the overall "size" of the octapeptide in solution. This quantity, as shown in the top panel in Figure 4, shows a distinct oscillation about two different types of minima: an open (or unfolded) structure, where $r_{cn} \approx 16$ Å, and a closed (or folded) structure, with $r_{cn} \approx 8$ Å. We also consider the HB populations by counting the number of HBs between the peptide backbone itself, n_{int}, and between peptide backbone and solvent, n_{ps}. Note that in the case of CHARMM there are water molecules bridging different amino acids of the peptide. These are counted in addition to direct peptide−peptide HBs to n_{int}. An HB is assigned as present if the acceptor−hydrogen distance is smaller than 2.7 Å (for n_{int}) or 2.4 Å (for n_{ps}) and the donor−hydrogen−acceptor angle is within 50 of linearity. The two classes of structures are characterized as open/closed by differing numbers of HBs, n_{ps} and n_{int}; see the two middle panels in Figure 4. The closed structures exhibit both types of HBs whereas the open structures feature only a few intrapeptide HBs and an extensive number of HBs to the solvent. This finding is in accord with observed isobestic points in the IR spectra and isodichroic points in the CD spectra, both of which signal the presence of a two-state system.[9,25,26]

It is stressed that the classification of a configuration as an open or closed conformation refers to a family of structures with similar structural characteristics; i.e., each class represents a myriad of local minima on the free energy surface. Typical configurations of both open and closed conformations are depicted in Figures 5a and 5b, respectively. Although the relative occurrence of open/closed structures differs from one simulation to the next and the details of the conformations between the
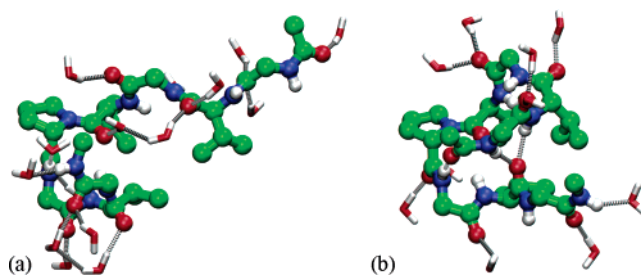
open and the closed forms depend on the force field (see below for further discussion), the existence of these two forms is generic to *all* of the force fields at *all* temperatures. Hence the following discussion will be cast in terms of these two structure classes.

As a next step, to probe the structural transition of this elastin-like octapeptide *systematically*, we consider the temperature dependence of the average value of r_{cn}, n_{ps}, and n_{int} as plotted in Figure 6 for all three force fields. At first glance, the temperature dependence of $\langle r_{cn} \rangle$ in Figure 6a is quite distinct for each of the three force fields. Specifically CHARMM shows the largest $\langle r_{cn} \rangle$ with an overall *decreasing* value as temperature increases, whereas GROMOS has the smallest value with an overall *increase* at higher temperatures. The OPLS simulations exhibit intermediate values of $\langle r_{cn} \rangle$ that are *decreasing* up to about 320 K then slowly *increasing* at higher temperatures. The obtained values of $\langle r_{cn} \rangle$ depend on both the number of open/closed species as well as their actual conformations, which depend on the force field characteristics. In general, GROMOS provides both open and closed structures with smaller r_{cn} values than CHARMM or OPLS with an increasing number of open species at higher temperatures. CHARMM also exhibits more open species at high temperatures, but these are not as extended as the ones observed at lower temperatures and hence result in a smaller average extension as measured by $\langle r_{cn} \rangle$. Despite these differences, closer examination of the data shows that, well within the approximate error bars, the evolution of $\langle r_{cn} \rangle$ is discontinuous in the range of 320−340 K for all three force fields with a pronounced shift to smaller values owing to a shift toward a higher population of the folded state.

This situation is mirrored by the behavior in the average populations of the various types of HBs. All three models show a decreasing trend $\langle n_{ps} \rangle$ as temperature is increased with, most importantly, a pronounced *discontinuous behavior* in the same temperature range, around 320−340 K; see Figure 6b. Likewise, $\langle n_{int} \rangle$ also evolves *discontinuously* with an increase around the structural transition *for all three force fields*, which corresponds to a relative increase of folded species around the transition temperature; see Figure 6c. Thus, despite the clear differences between the various simulation schemes, all three show signs of a temperature-dependent structural transition, similar to our previous results,[25,31] at temperatures above ambient.

Further information about the peptide backbone conformations can be obtained by examining Ramachandran plots (data not shown) of the torsional angles ψ and ϕ about peptide bonds to spot possible conformational preferences of the various force fields.[42] In all three force fields used, the proline amino acid displays similar conformations with two main peaks with the largest populations occurring at about $\psi = 155°$ and $\phi = -75°$ and a lower density peak around $\psi = -30°$ and $\phi = -80°$. We

ITT of a Biomimetic Elastin Model
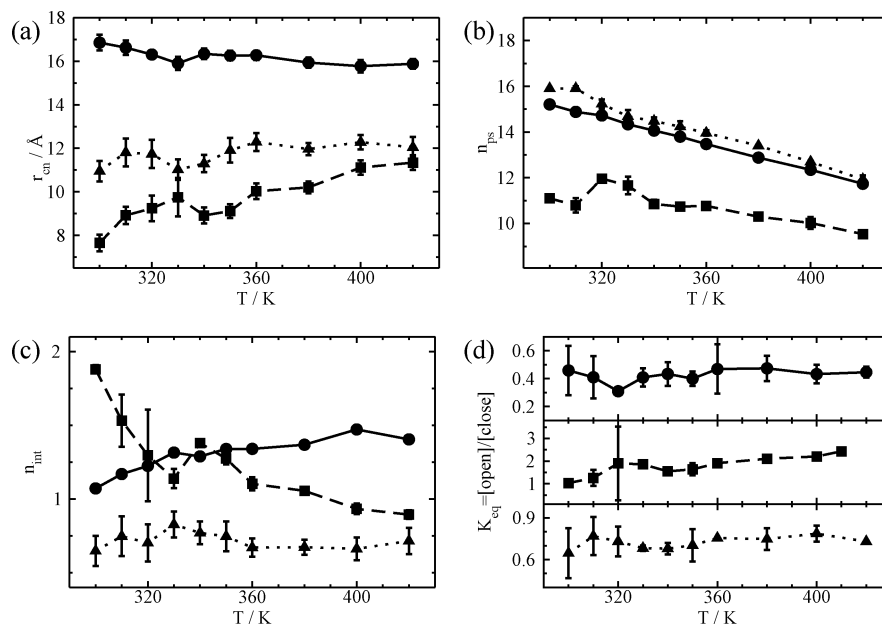
J. Phys. Chem. B, Vol. 110, No. 8, 2006 **3581**

Figure 6. Average quantities as a function of temperature: (a) end-to-end distance, $\langle r_{cn} \rangle$; (b) number of peptide−solvent HBs, $\langle n_{ps} \rangle$; (c) number of peptide−peptide HBs, $\langle n_{int} \rangle$; (d) equilibrium constant, $K_{eq} = [o]/[c]$, as a function of temperature. See section 2.5 for definitions. Data sets are given for the CHARMM (circles), GROMOS (squares), and OPLS (triangles) force fields.

note that the CHARMM force field exhibits a well-resolved shoulder about the former peak ($\psi = 85°$ and $\phi = -75°$) but still retains the two main peaks at the same location as the other two force fields. The observed conformations demonstrate that in terms of the conformations about the central proline residue all methods provide *qualitatively* the same configurations in about the same proportion. We note that the same conformations appear at both high and low temperatures with differing populations but no additional peaks, which suggests that our simulations have explored the relevant conformations at all temperatures.

Not all the amino acids, however, exhibit the same conformations when comparing different force fields.[42] This is most noticeable for Gly6, which is located next to the proline in the repreat unit of GVG(VPGVG). The CHARMM potential shows only one prominent conformation at approximately $\psi = 165°$ and $\phi = 165°$, which appears at both high and low temperatures, indicating a sufficient conformational space sampling of our simulations. In combination with the proline dihedrals this conformation does not correspond to any well-defined structural motif and might be best classified as random coil structure. However, both the OPLS and the GROMOS simulations show several conformations not thermally accessible to the CHARMM potential. The OPLS trajectories display two pronounced peaks at positions around $\psi = 165°$, $\phi = -125°$ and $\psi = -15°$, $\phi = 105°$. Given the proline dihedrals, these configurations may be attributed to β-VIII and β-II turns, respectively. Additionally, two peaks are found at $\psi = 0°$, $\phi = -120°$ and $\psi = -175°$, $\phi = 105°$ and might be best classified as random coil structures. Also GROMOS exhibits four distinct conformations, located at $\psi = -85°$, $\phi = -75°$; $\psi = -90°$, $\phi = 75°$; $\psi = 20°$, $\phi = 55°$; and $\psi = 85°$, $\phi = -85°$. In conjunction with the proline angles the latter may represent a β-V turn, whereas the other three describe random coil structures. Again, these structures are present at all temperatures, however, with different associated weights. Similar structural motifs were indeed found experimentally.[9,23−26,28,77] In addition these studies suggest a dynamic equilibrium between the various structures that depends on the temperature. In passing, it is noted that secondary

structure motifs in short, highly dynamic peptides, such as the octapeptide studied here, are only of limited diagnostic use.

One consequence of these observations is that the CHARMM potential, which exhibits overall stiffer dihedral potentials than the other force fields, has a more restricted conformational space and thus requires shorter simulation times for sufficient sampling. However, the additional conformations available to GROMOS and OPLS require larger simulation times to converge the simulations due to both the lower frequency vibrational motion of the backbone and the larger conformation space that needs to be sampled. To resolve which, if any, of the different force fields is the most appropriate for this problem also in quantitative terms, a detailed comparison with NMR studies is required, which is currently ongoing but beyond the scope of the present paper. Most importantly for the current objective, all simulations show open and folded structures, including a systematic change of their relative weights as a function of temperature, although the actual conformations of these structures and their relative populations do strongly depend on the force field model.

3.2. Conformational Dynamics and Free Energies. To probe the above findings in a systematic but simple way, one would ideally want to describe the conformational behavior using a single, well-defined "order parameter". Following our previous work,[25,31] we have employed the PCA as outlined in subsection 2.5. Note that to converge the results for this analysis, it has proven necessary to obtain longer simulations with GROMOS and OPLS due to the above observation that a larger conformational space needs to be explored for these force fields; in particular the GROMOS force field required at least 40 ns to show convergence in the lowest eigenmode, $\mathbf{m}_1$. The observation that slow convergence of PCA results even for small peptides underscores the necessity to perform very careful convergence checks to guarantee the reliability of the obtained modes.

After careful convergence of the data, all three force fields yield a lowest eigenmode, $\mathbf{m}_1$, which is found to be the *same* at all temperatures as characterized by the dot products between the modes at different temperatures, which are typically 0.9 or
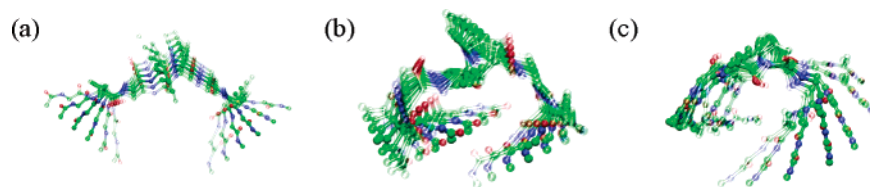
Figure 7. Schematic representation of the largest-amplitude PCA eigenmode, $\tilde{\mathbf{m}}_1$, from the covariance analysis: (a) CHARMM, (b) GROMOS, and (c) OPLS. The renderings were obtained by scanning the accessible amplitude of the first eigenvector from the corresponding trajectory at 300 K in equidistant increments. For a dynamical visualization, see ref 78.

greater. This means that our adoption of a uniform eigenmode basis, $\{\tilde{\mathbf{m}}_i\}$, for each simulation scheme does not affect the accuracy of our representation of the dynamics with respect to the lowest eigenmode. The motion along the mode $\tilde{\mathbf{m}}_1$, depicted graphically in Figure 7 and visualized dynamically in ref 78, has the property that it connects the open and closed structures continuously and is well-correlated to the changes in HB numbers and r_{cn} according to the lowest panel of Figure 4. Overall the mode $\tilde{\mathbf{m}}_1$ accounts for approximately 38%, 27%, and 33% of the total variance of the peptide backbone motion for CHARMM, GROMOS, and OPLS, respectively, hence capturing a sizable proportion of the large-amplitude peptide dynamics all within a single variable. The distribution, $P(\tilde{m}_1)$, of the projection on the first eigenmode (see subsection 2.5) is bimodal for all three models whereas all other modes are essentially unimodal at all temperatures (data not shown), with the exception of the CHARMM data between 300 and 350 K, which exhibit a shoulder in $P(\tilde{m}_2)$. It is noted that an identical largest-amplitude mode was also observed in our previous EGO study[25,31] of this peptide. Overall, $\tilde{m}_1$ can be used as a valuable order parameter as it describes the *majority* of the crucial components of the peptide dynamics, i.e., the "essential dynamics". As a result, it can be analyzed to extract fundamental thermodynamical quantities, such as relative free energies and equilibrium constants, which characterize this particular conformational transition.

In view of the force field differences as discussed in terms of backbone conformations in subsection 3.1, it is at this stage instructive to check how similar the mode $\tilde{\mathbf{m}}_1$ is when comparing the force fields. As can be inferred from Figure 7, all three force fields qualitatively exhibit open/closing modes where the proline acts like a "hinge". This correlates well with the observation of very similar dihedral angles ψ and ϕ for this amino acid in all three models. To quantify this we consider the dot product between $\tilde{\mathbf{m}}_1$ as obtained from each force field. If the motion is exactly the same, then the modulus of the dot product will be unity, and if the vectors are orthogonal, then it will be zero. Between CHARMM and OPLS this dot product is about 0.8 whereas between OPLS and GROMOS the dot product is 0.12 with a similarly small value between CHARMM and GROMOS. However, most of the deviation between these modes arises from the peptide's termini, which are found to have increased mobility when going from CHARMM to OPLS to GROMOS. Most importantly, it can be gleaned from the schematics in Figure 7 that the GROMOS $\tilde{\mathbf{m}}_1$ mode in part b has a more complex nature involving not only a bending but also a significant twisting component when directly compared to CHARMM in part a or OPLS in part c, whereas these modes are qualitatively very similar. Together with the flexibility at the ends, this causes the projection of the GROMOS $\tilde{\mathbf{m}}_1$ mode onto the respective CHARMM and OPLS modes to degrade. Again, this correlates well with our above observations regarding the rigidity of the peptide backbone as parametrized for each force field. It is concluded that the lowest mode $\tilde{\mathbf{m}}_1$ is very similar for

CHARMM and OPLS but *quantitatively* different compared to GROMOS, although in the latter case the motion is *qualitatively* also of an opening/closing type as in the other cases. Hence, upon careful convergence of the results it is uncovered that all three force fields show a similar collective dynamics interconnecting open and closed conformations.

As a next step, we consider free energy profiles defined by $G(\tilde{m}_1) = -k_{B}T \ln(P(\tilde{m}_1)/P(\tilde{m}_1^0))$, where $P(\tilde{m}_1^0)$ is some reference value of the underlying order parameter distribution function $P(\tilde{m}_1)$; see Figures 8a−c. In all three simulations two minima exist as a function of $\tilde{m}_1$, with the closed structures located at negative and open structures at positive $\tilde{m}_1$ values. For all three force fields the global minimum of $G(\tilde{m}_1)$ is a closed structure, and the open structures are local minima with free energy differences, $\Delta G = G(\tilde{m}_1^{closed}) - G(\tilde{m}_1^{open})$, typically of a few kJ mol^{-1}; see Figure 8d. As temperature increases the relative free energy of the closed structures decreases. In all cases this would correspond to an increase in open structures at high temperatures and would account for the *unfolding* for $T > 360$ K as previously observed experimentally for this very system[25,26] in which ΔG was estimated to be of the order of only a few kcal mol^{-1}. Moreover, the decreasing free energy of the open state is not monotonic, and all three simulation schemes show an *intermediate regime* where ΔG shows an increased preference for folded states between 320 and 360 K, depending on the force field. This regime corresponds to the experimentally observed ITT[9,25,26] and is present in *all simulations*, including our previous ones.[25,31]

As a complementary refinement of this analysis, it is noted that the two states observed in $G(\tilde{m}_1)$ allow us to define an approximate transition state, $\tilde{m}_1^{\ddagger}$, for each simulation as outlined in subsection 2.5. Integrating $P(\tilde{m}_1)$ up to (from) $\tilde{m}_1^{\ddagger}$ allows us to obtain the concentration estimates of closed (open) species, [c] ([o]), and thus to define an equilibrium constant, $K_{eq} = [o]/[c]$, that is depicted in Figure 6d as a function of temperature. At all temperatures GROMOS shows the lowest concentration of closed structures whereas CHARMM shows the highest. This is despite the fact that GROMOS exhibits a deep minimum at $T < 320$ K for these conformations because the majority of the density is spread out over the comparatively broad configuration space of open states. Again all three force fields show an overall increase in K_{eq} at the highest temperatures, corresponding to an unfolding regime, but there is a pronounced dip between $T = 320$ and 360 K owing to an increase in folded structures. This is a clear signal of an ITT, that is an increased *folding* upon *increasing* the temperature above ambient. In agreement with our earlier results[25,31] the temperature range with increased concentration of folded structures is small (CHARMM, 320−330 K; GROMOS, 350−360 K; OPLS, 330−350 K) and also depends on the force field.

This picture compares favorably with that obtained from the IR and CD data reported earlier.[25,26] As stated previously, the existence of the isobestic/isodichroitic points indicates the

ITT of a Biomimetic Elastin Model
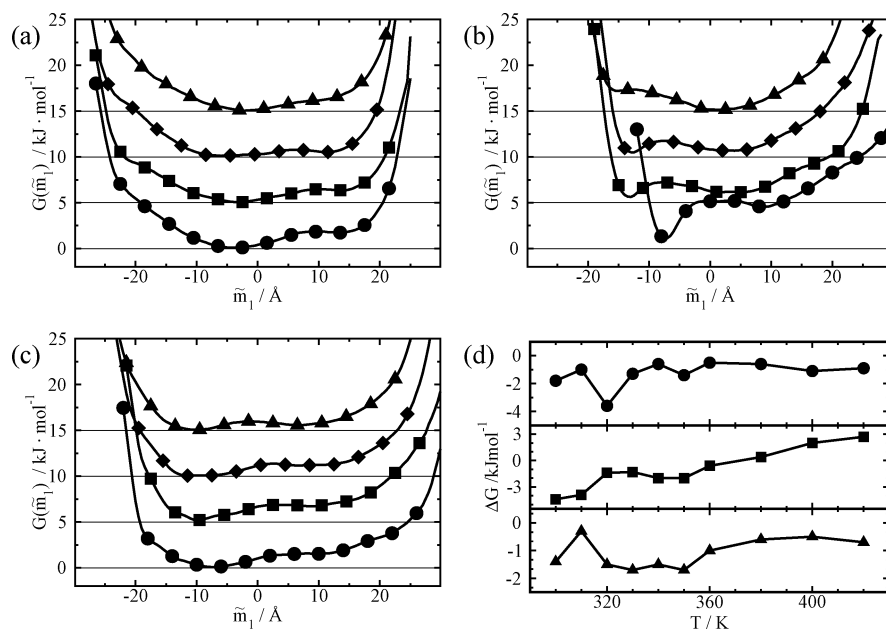
J. Phys. Chem. B, Vol. 110, No. 8, 2006 **3583**

Figure 8. Free energy profile, $G(\tilde{m}_1)$, for several temperatures using (a) CHARMM, (b) GROMOS, and (c) OPLS. Temperatures shown are 300 K (circles), 330 K (squares), 360 K (diamonds), and 400 K (triangles); data for successive temperatures are shifted in increments of 5 kJ mol^{-1} for clarity. (d) Free energy difference between open and closed conformations, ΔG, as a function of temperature using CHARMM (circles), GROMOS (squares), and OPLS (triangles).

existence of two species at all temperatures, with the relative concentrations showing a temperature dependence. Analysis of the spectra suggests that structural motifs associated with more closed conformations *increase* in population up until around 340 K and decrease at higher temperatures, with the converse occurring for more open forms. The estimated activation free energy for this process was only 1–2 kcal mol^{-1}, in agreement with the small barriers observed in the current study. The reported potential energy surfaces with broad minima and small potential energy barriers also correlate well with the rapid dynamical equilibrium and large chain mobility observed in various NMR measurements of similar systems.[18–23]

Overall, despite all the differences in the details of the conformations between the various models worked out in subsection 3.1, the present thermodynamics analysis shows that *all* force fields feature an ITT. Specifically, all three show essentially a two-state system consisting of open and closed structures connected by an order parameter $\tilde{m}_1$ with an increase of the latter conformations in intermediate temperature regimes, i.e., an ITT. The ability of a force field to actually reproduce the exact structure of the solvated elastin octapeptide is still an open issue awaiting more definitive experimental characterization, which is ongoing. However, the fact that all three simulations *do* exhibit qualitatively the same transition argues that the structural transition does not depend on the fine details of the force field but rather is governed by more general features, such as solvent fluctuations and the peptide–solvent interactions. In the next subsection we will consider this observation in more detail first from a dynamic and then from a kinetic perspective.

3.3. Solvent Dielectric Relaxation and Peptide Folding/ Unfolding. In this subsection we shift our focus to considering dynamic quantities with the specific goal of probing the role of the peptide–water interaction in the observed structural transition. From our previous work an interesting reciprocity arose between the picosecond dynamics of the peptide–solvent HB dynamics and the nanosecond peptide backbone folding/ unfolding dynamics.[25,31] However, here we choose to take a more coarse-grained approach and consider the solvent solely in terms of its dielectric relaxation, inspired by interesting

experimental findings.[32] Hence, the focus is on the dynamics of the peptide along the reaction coordinate and on determining how this large-scale collective motion is influenced by the microscopic fluctuations of the solvent.

The dynamical motion of the peptide backbone along the reaction coordinate, $\tilde{m}_1$, can be best quantified by considering the system as consisting of two states closed (c) and open (o), which are in dynamic equilibrium via forward (i.e., unfolding c → o) and reverse (i.e., folding c ← o) reactions (i.e., conformational changes) with the rate constants k_{uf} and k_f, respectively. As described earlier the two species are separated along the reaction coordinate by a transition state, $\tilde{m}_1^{\ddagger}$, which forms a dividing surface between the two states. This description allows us to formulate a reactive flux correlation function (see subsection 2.5), $k_{uf/f}(t)$, where the rate constants, $k'_{uf/f}$, are obtained from a plateau value of this function for t greater than the internal relaxation time of the peptide, τ_p. Illustrative examples of these functions as obtained from the representative $T = 300$ K OPLS trajectory are displayed in Figure 9a, which shows with a few hundred crossings, even for the relatively low-temperature runs, that our statistics are sufficiently converged to obtain well-defined plateaus, and thus rate constants, for times $t > 0.2$ ns. As a cross check on the reliability of the obtained rate constants, we note that the relation $K_{eq} = [o]/[c] = k'_{uf}/k'_f$ must hold. The ratio of the computed rate constants provides us with K_{eq} values (data not shown) with the same temperature dependence as those extracted directly from free energy differences and reported in Figure 6d. Most noticeable is the increase of folded species at the ITT, which confirms that our data are sufficiently converged to allow us to elucidate the transition mechanism from a kinetics perspective.

To understand the temperature dependence of the various reaction rates of the *peptide* we present the data in terms of an Arrhenius plot, $\ln(k'_{uf/f})$ versus $1/T$ in Figure 9b. In all cases, the obtained rate constants can be considered to consist of *three* temperature regimes: low-temperature regime, ITT regime, and high-temperature regime. Note that the kinetics analysis of interfacial *water* in our earlier work[25,31] could not resolve the
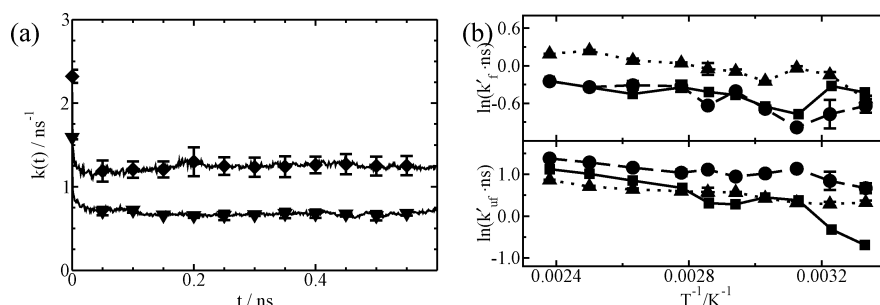
Figure 9. (a) Reactive flux correlation function for folding, $k_f(t)$ (diamonds), and unfolding, $k_{uf}(t)$ (triangles), shown as a function of time for the OPLS trajectory at 300 K. See Figure 4 for the corresponding time evolution of $\tilde{m}_1$. (b) Arrhenius plots of the folding and unfolding rates, k'_f (top) and k'_{uf} (bottom), using CHARMM (circles), GROMOS (squares), and OPLS (triangles).

ITT regime and only yielded what has been called "folding" and "unfolding" regimes below and above a certain temperature. Below the ITT, both folding and unfolding rates are smaller than those at high temperatures but have a larger slope due to the relatively high free energy difference of open versus closed species; see Figure 8d. However, we point out that the data at lower temperatures are not sufficiently converged to determine without doubt if there is indeed an Arrhenius behavior. Around the ITT temperatures there is a discontinuity and above the ITT regime the data sets are sufficiently converged to show Arrhenius behavior with a smaller slope than that at low temperatures owing to the flatter free energy surface. Thus, the rate constant data reflect—within the given error bars—the scenario obtained from the structure and energetics as worked out in the previous sections.

At this point, we briefly digress to consider peptide dynamics being possibly slave modes of *bulk* water, as proposed by Fenimore et al.;[32] for a complementary discussion based on the theory of glass-forming liquids we refer to ref 79, and for a related analysis of the role of dielectrics, see ref 80. The concept of "slaving" refers to a process whereby the solvent fluctuations, possibly, overwhelm those of the peptide and hence govern its fluctuations and, more importantly, folding kinetics. A qualitative but simple argument goes back to the fact that the dielectric constant for *neat* water, $\epsilon_s \propto (\Delta \mathbf{M}_s)^2 \approx 80$, is much larger than that of the peptide, $\epsilon_p \propto (\Delta \mathbf{M}_p)^2 \approx 1{-}10$, where $(\Delta \mathbf{M}_{s/p})^2 = \langle \mathbf{M}_{s/p}^2 \rangle - \langle \mathbf{M}_{s/p} \rangle^2$ are the fluctuations of the instantaneous water/peptide dipole $\mathbf{M}_{s/p}(t)$, (see refs 72 and 73 for a discussion of peptide dielectrics). As a result, the large instantaneous dipole of the solvent can couple with that of the peptide and thereby control its dynamics. Finally, as discussed by Berry and co-workers,[80,81] the electrostatics of slaving is intimately tied to the fluctuations of the HB network.

Previously we found preliminary evidence for such a coupling in view of the distinct change of the HB kinetics of *interfacial* water in the folding and unfolding regimes.[25,31] In the current simulation, we find $(\Delta \mathbf{M}_s)^2$ approximately 40–80 times larger than $(\Delta \mathbf{M}_p)^2$ in all simulations. To *qualitatively* evaluate how the solvent fluctuations may couple with those of the peptide we consider a single peptide dipole, $\mathbf{M}_p$, interacting with the fluctuating total dipole of the solvent, $\mathbf{M}_s$, where *all water molecules* are considered in the spirit of the slave mode concept; we leave the known subtleties[73] involved in such partitioning schemes to future investigations. The approach is approximate by construction, neglecting in particular the effects of the local electric field fluctuations near the peptide, but provides us with a simple measure for the dipole—dipole interaction between solvent and peptide, which is proportional to the average of the scalar product of these two vectors, $\langle \mathbf{M}_s \cdot \mathbf{M}_p \rangle$; see ref 72. It is noted that calculation of the time-dependent cross-correlation
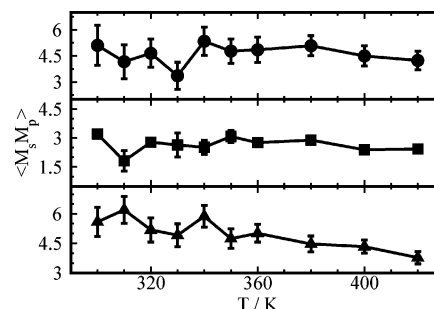

Figure 10. Static component of the solvent—peptide dipole cross correlation, $\langle \mathbf{M}_s \cdot \mathbf{M}_p \rangle$, as a function of temperature using CHARMM (circles), GROMOS (squares), and OPLS (triangles); compare with Figure 6.

function, $\langle \mathbf{M}_s(0) \cdot \mathbf{M}_p(t) \rangle$, to evaluate the time-dependent portion of the coupling was numerically not well converged, even for these relatively long trajectories, and thus we formulate our discussion solely in *qualitative* terms based on the static component, $\langle \mathbf{M}_s(0) \cdot \mathbf{M}_p(0) \rangle$, as depicted in Figure 10. Unlike the two self-terms, $\langle \mathbf{M}_s^2 \rangle$ and $\langle \mathbf{M}_p^2 \rangle$, which show smooth temperature variations (data not shown), the cross term $\langle \mathbf{M}_s \cdot \mathbf{M}_p \rangle$ shows a more complex variation where coupling is—within the error bars—at least a local maximum within the ITT regime for all three force fields; compare with Figure 6d. Moreover, since the largest-amplitude motions of the peptide are contained, by construction, within the reaction coordinate $\tilde{m}_1$, the fluctuations of the peptide dipole can thus be directly correlated with its open/closing conformational motion. These observations suggest the possibility that a slave mode type mechanism may be operative in this system and that it may be related to the ITT. Hence, the *kinetics* of folding/unfolding of the peptide and its correlation with the solvent dielectric relaxation should provide insights into the role of the solvent in the ITT, in particular if solvent fluctuations influence peptide motion or *vice versa*.

To work out and quantify this scenario in terms of statistical mechanics we consider the dynamical fluctuations of the solvent as described by its dielectric relaxation rate, k_{diel}, introduced in subsection 2.5. We obtain this quantity by calculating the total dipole—dipole autocorrelation function for the bulk solvent and fitting it to a simple Debye relaxation model, $\exp[-t/\tau_{diel}]$. The resulting total water rates are essentially identical between CHARMM and OPLS, because both water models, TIPS3P and TIP3P, have the same charge distribution and interatomic distances; SPC water used in the GROMOS simulations yields slightly larger relaxation rates. A plot of $\ln k_{diel}$ versus $1/T$, as shown in Figure 11a, shows that the bulk water relaxation time exhibits a clear Arrhenius behavior in the *entire* temperature range probed. Thus it is indeed acting predominantly like bulk
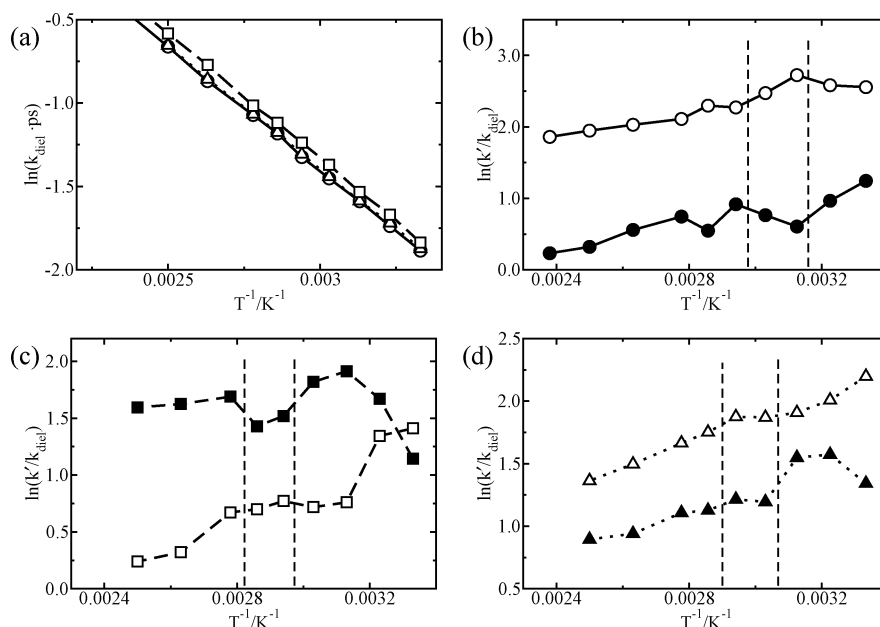
ITT of a Biomimetic Elastin Model

J. Phys. Chem. B, Vol. 110, No. 8, 2006 **3585**

Figure 11. (a) Arrhenius plot of the dielectric relaxation rate for solvent water, k_{diel}, using CHARMM (circles), GROMOS (squares), and OPLS (triangles). Estimated error bars are of the order of the symbol sizes. Arrhenius plot of ratios k'_f/k_{diel} (open symbols) and k'_{uf}/k_{diel} (filled symbols) using (b) CHARMM (circles), (c) GROMOS (squares), and (d) OPLS (triangles). Vertical lines mark the approximate temperature boundaries of the ITT regime; see text and Figure 6d, and error bars may be estimated from the data in Figure 9.

water, in accordance with previous theoretical[82−85] and experimental[85−88] studies.

To see how the rates of the folding/unfolding of the peptide compare with those of the solvent fluctuations we consider the ratio $k'_{uf/f}/k_{diel}$ as given in Arrhenius plots in Figures 11b−d. A flat region in the plot of ln $k'_{uf/f}/k_{diel}$ would indicate a similar free energy barrier between solvent and peptide fluctuations and hence slave mode behavior resulting from a strong dipolar coupling between the two processes. For all three force fields, this quantity shows three clear temperature regimes with boundaries corresponding to observed changes in K_{eq} as can be seen by comparing with Figure 6d. Below the ITT there is no correlation with either rate or solvent fluctuations. Rates of folding are increasing slower than the increase in dielectric relaxation in all simulations, whereas the unfolding process behaves differently between the simulation types. Likewise, in the high-temperature regime the temperature dependence of both folding and unfolding are all decreasing slower than those of the solvent. However, in the intermediate regime, that is in the ITT regime, both OPLS and GROMOS show a change in rate that is concurrent with that of the solvent fluctuations, which *might suggest* slave mode type behavior.[32] For CHARMM the situation is a bit different in that although ln $k'_{uf/f}/k_{diel}$ shows discontinuous behavior, a well-resolved plateau region is not apparent from the data. This discrepancy may arise either from the approximation of using $\tilde{m}_1$ as an order parameter, which is less accurate for CHARMM in this temperature range as discussed in subsection 3.1, or from the fact that the ITT regime is very narrow for CHARMM according to Figure 6d in that only the 320 K data point shows a significant increase in folded structures. Most importantly, in all three cases the data indicates that concurrent with the ITT there may be a characteristic change between the coupling of the peptide dipole and the dielectric fluctuations of the bulk solvent.

Taken together, our accumulated evidence suggests that the observed ITT in these systems may be a result of increased coupling between *bulk* solvent fluctuations and those of the peptide dipole at temperatures slightly above ambient where folding and ultimately the ITT takes place. Clearly, this

suggestion has to be scrutinized using better statistics, i.e., longer simulations, and longer peptide chains, i.e., more repeat units in GVG(VPGVG)$_n$. This novel view is certainly complementary to others, such as our previous kinetics analysis of *interfacial* HB fluctuations[25,31] as well as more established pictures of the ITT as reviewed in these publications and in the introduction of this study.

4. Conclusions and Outlook

In this paper we have investigated the so-called inverse temperature transition (ITT) of an elastin biomimetic, the capped octapeptide GVG(VPGVG), solvated explicitly by about 4000 water molecules, with three distinct force field models, CHARMM-22/TIPS3P, GROMOS-43a1/SPC, and OPLS-AA/L/TIP3P. The data analysis is based on well-equilibrated constant pressure/temperature molecular dynamics trajectories on the order of 100 ns, each at about 10 temperatures, adding up to several microseconds of simulation time. Despite the fact that the detailed conformations of the octapeptide do differ among the simulation schemes, they exhibit a very similar behavior with respect to a *qualitative classification* as either closed (folded) or open (unfolded), confirming our previous study.[25,31,48] Currently, a joint experimental−theoretical study is under way to further scrutinize the different force fields in *quantitative* terms. Most notably, however, the dynamics of the peptide may be reasonably well described by an order parameter that connects the two states (open/closed) for all force fields, featuring an *increase of folded structures upon increasing temperature*, i.e., an ITT, in a force-field-dependent temperature range above 320 K. The ITT and low- and high-temperature regimes can be analyzed in terms of free energy differences between closed and open states and corresponding equilibrium constants as a function of temperature.

A first indication on changes in the solvent−peptide coupling during folding/unfolding is obtained by analyzing the cross correlation between solvent and peptide dipole moments, which features a local minimum at about the ITT temperature regime for all force fields. Furthermore, comparison of the temperature

dependence of the peptide folding/unfolding rates (extracted from the reactive flux approach to peptide kinetics) to the dielectric relaxation rate of water (obtained from the total dipole autocorrelation function of the *bulk* solvent), showed a distinct change in the peptide−solvent dipole coupling setting in with the ITT. This *might* be a first indication of a slave mode[32] type behavior in the temperature regime above the ITT. Confirmation of this finding would be obtained, e.g., by a detailed study of the dielectric relaxation spectrum as a function of temperature. Future theoretical work will focus on extending these findings to obtain a more *quantitative* understanding of the mechanism of the ITT in this system. For this purpose, specific mutants known to suppress the ITT will be the ideal probe.

More generally speaking, we advocate these capped elastin biomimetics, Ac-GVG(VPGVG)$_n$-Me, as ideal models of controllable complexity to study *both* folding and unfolding of proteins as a function of length n in a regime—water at ambient conditions—that is conveniently accessed experimentally as well as it is probed computationally.

References and Notes

(1) Pasquali-Ronchetti, I.; Fornieri, C.; Baccarani-Contri, M.; Quaglino, D. Ultrastructure of elastin. In *The Molecular Biology and Pathology of Elastic Tissues*; John Wiley & Sons: New York, 1995.

(2) Debelle, L.; Alix, A. J. P. *Biochimie* **1999**, *81*, 981−994.

(3) Debelle, L.; Tamburro, A. M. *Int. J. Biochem. Cell Biol.* **1999**, *31*, 261−272.

(4) Martino, M.; Perri, T.; Tamburro, A. M. *Mol. Biosci.* **2002**, *2*, 319−328.

(5) Reiersen, H.; Rees, A. R. *Trends Biochem. Sci.* **2001**, *26*, 679−684.

(6) Urry, D. W. *J. Phys. Chem. B* **1997**, *101*, 11007−11028.

(7) Urry, D. W.; Hugel, T.; Seitz, M.; Gaub, H. E.; Sheiba, L.; Dea, J.; Xu, J.; Parker, T. *Philos. Trans. R. Soc. London, Ser. B* **2002**, *357*, 169−184.

(8) Urry, D. W. *Angew. Chem., Int. Ed.* **1993**, *32*, 819−841.

(9) Reiersen, H.; Clarke, A. R.; Rees, A. R. *J. Mol. Biol.* **1998**, *283*, 255−264.

(10) Nath, N.; Chilkoti, A. *J. Am. Chem. Soc.* **2001**, *123*, 8197−8202.

(11) Wright, E. R.; Conticello, V. P. *Adv. Drug Delivery Rev.* **2002**, *54*, 1057−1073.

(12) Urry, D. W.; Long, M. M.; Sugano, H. J. *J. Biol. Chem.* **1978**, *253*, 6301−6302.

(13) Cook, W. J.; Einspahr, H. M.; Trapane, T. L.; Urry, D. W.; Bugg, C. E. *J. Am. Chem. Soc.* **1980**, *102*, 5502−5505.

(14) Li, B.; Alonso, D. O. V.; Benion, B. J.; Daggett, V. *J. Am. Chem. Soc.* **2001**, *123*, 11991−1198.

(15) Hoeve, C.; Flory, P. J. *Biopolymers* **1974**, *13*, 677−686.

(16) Wasserman, Z. R.; Salemme, F. R. *Biopolymers* **1990**, *29*, 1613−1631.

(17) Partridge, S. *Adv. Protein Chem.* **1962**, *17*, 227−302.

(18) Fleming, W. W.; Sullivan, C. E.; Torchia, D. A. *Biopolymers* **1980**, *19*, 597−617.

(19) Torchia, D. A.; Piez, K. A. *J. Mol. Biol.* **1973**, *76*, 419−424.

(20) O. Arad, M. G. *Biopolymers* **1990**, *29*, 1651−1668.

(21) Urry, D. W.; Trapane, T. L.; Iqbal, M.; Venkatachalam, C. M.; Prasad, K. U. *Biochimie* **1985**, *24*, 5182−5189.

(22) Perry, A.; Stypa, M. P.; Foster, J. A.; Kumashiro, K. K. *J. Am. Chem. Soc.* **2002**, *124*, 6832−6833.

(23) Kurková, D.; Kříž, J.; Schmidt, P.; Dybal, J.; Rodríguez-Cabello, J. C.; Alonso, M. *Biomacromolecules* **2003**, *4*, 589−601.

(24) Debelle, L.; Alix, A. J. P.; Jacob, M. P.; Huvenne, J. P.; Berjot, M.; Sombret, B.; Legrand, P. *J. Biol. Chem.* **1995**, *270*, 26099−26103.

(25) Schreiner, E.; Nicolini, C.; Ludolph, B.; Ravindra, R.; Otte, N.; Kohlmeyer, A.; Rousseau, R.; Winter, R.; Marx, D. *Phys. Rev. Lett.* **2004**, *92*, 148101.

(26) Nicolini, C.; Ravindra, R.; Ludolph, B.; Winter, R. *Biophys. J.* **2004**, *86*, 1385−1392.

(27) Schmidt, P.; Dybal, J.; Rodríguez-Cabello, J. C.; Reboto, V. *Biomacromolecules* **2005**, *6*, 697−706.

(28) Ohgo, K.; Ashida, J.; Kumashiro, K. K.; Asakura, T. *Macromolecules* **2005**, *38*, 6038−6047.

(29) Li, B.; Alonso, D. O. V.; Daggett, V. *J. Mol. Biol.* **2001**, *305*, 581−592.

(30) Li, B.; Daggett, V. *Biopolymers* **2003**, *68*, 121−129.

(31) Rousseau, R.; Schreiner, E.; Kohlmeyer, A.; Marx, D. *Biophys. J.* **2004**, *86*, 1393−1407.

(32) Fenimore, P. W.; Frauenfelder, H.; MacMahon, B. H.; Parak, F. G. *Proc. Natl. Acad. Sci. U.S.A.* **2002**, *99*, 16047−16051.

(33) Laio, A.; Parrinello, M. *Proc. Natl. Acad. Sci. U.S.A.* **2002**, *99*, 12562−12566.

(34) Grubmüller, H. *Phys. Rev. E* **1995**, *52*, 2893−2906.

(35) Anderson, J. B. *Adv. Chem. Phys.* **1995**, *91*, 381−431.

(36) Saiz, L.; Bandyopadhyay, S.; Klein, M. L. *Biosci. Rep.* **2002**, *22*, 151−173.

(37) Saiz, L.; Klein, M. L. *Acc. Chem. Res.* **2002**, *35*, 482−489.

(38) MacKerell, A. D., Jr.; Bashford, D.; Bellott, R. L.; Dunbrack, R. L., Jr.; Evanseck, J. D.; Field, M. J.; Fischer, S.; Gao, J.; Guo, H.; Ha, S.; Joseph-McCarthy, D.; Kuchnir, L.; Kuczera, K.; Lau, F. T. K.; Mattos, C.; Michnick, S.; Ngo, T.; Nguyen, D. T.; Prodhom, B.; Reiher, W. E., III; Roux, B.; Schlenkrich, M.; Smith, J. C.; Stote, R.; Straub, J.; Watanabe, M.; Wiorkiewicz-Kuczera, J.; Yin, D.; Karplus, M. *J. Phys. Chem. B* **1998**, *102*, 3586−3616.

(39) van Gunsteren, W. F.; Billeter, S. R.; Hünenberger, A. A.; Krüger, P.; Mark, A. E.; Scott, W. R. P.; Tironi, I. G. *Biomolecular Simulation: The GROMOS96 Manual and User Guide*; Hochschulverlag AG an der ETH Zürich: Zürich, Switzerland, 1996.

(40) Damm, W.; Frontera, A.; Tirado-Rives, J.; Jorgensen, W. *J. Comput. Chem.* **1997**, *18*, 1955−1970.

(41) Mackerell, A. D., Jr. *J. Comput. Chem.* **2004**, *25*, 1584−1604.

(42) Mu, Y. G.; Kosov, D. S.; Stock, G. *J. Phys. Chem. B* **2003**, *107*, 5064−5073.

(43) Hu, H.; Elstner, M.; Hermans, J. *Proteins: Struct., Funct., Genet.* **2003**, *50*, 451−463.

(44) Paschek, D. *J. Chem. Phys.* **2004**, *120*, 6674−6690.

(45) Berendsen, H. J. C.; Postma, J. P. M.; F.van Gunsteren, W.; Hermans, J. *Proceedings of the 14th Jerusalem Symp. on Quantum Chem. and Biochem.*; Pullman, B., Ed.; Reichel: Dodrecht, Holland, 1981, pp 331−342.

(46) Jorgensen, W. L.; Chandrasekhar, J.; Madura, J. D.; Impey, R. W.; Klein, M. L. *J. Chem. Phys.* **1983**, *79*, 926−935.

(47) Durell, S. R.; Brooks, B. R.; Ben-Naim, A. *J. Phys. Chem* **1994**, *98*, 2198−2202.

(48) This simulation was done using the ego-VIII simulation package using the CHARMM-22 force field with very similar parameters to those of the present study, mainly differing in the use of droplet stochastic boundary conditions. See ref 31 for full details.

(49) Lindahl, E.; Hess, B.; van der Spoel, D. *J. Mol. Model.* **2001**, *7*, 306−317. http://www.gromacs.org/.

(50) Berendsen, H. J. C.; van der Spoel, D.; van Drunen, R. *Comput. Phys. Commun.* **1995**, *91*, 43−56.

(51) Hockney, R. W.; Goel, S. P. J. *J. Comput. Phys.* **1974**, *14*, 148.

(52) Hess, B.; Bekker, H.; Berendsen, H. J. C.; Fraaije, J. G. E. *J. Comput. Chem.* **1997**, *18*, 1463−1472.

(53) Miyamoto, S.; Kollman, P. A. *J. Comput.Chem.* **1992**, *13*, 952−962.

(54) Ryckart, J. P.; Cicotti, G.; Berendsen, H. J. C. *J. Comput. Phys.* **1977**, *23*, 327−341.

(55) Nosé, S. *Mol. Phys.* **1984**, *52*, 255−268.

(56) Hoover, W. G. *Phys. Rev. A* **1985**, *31*, 1695−1697.

(57) Parrinello, M.; Rahman, A. *J. Appl. Phys.* **1981**, *52*, 7182−7190.

(58) Nosé, S.; Klein, M. L. *Mol. Phys.* **1983**, *50*, 1055−1076.

(59) Darden, T.; York, D.; Pederson, L. *J. Chem. Phys.* **1993**, *98*, 10089−10092.

(60) Kaminski, G. A.; Friesner, R. A.; Tirado-Rives, J.; Jorgensen, W. L. *J. Phys. Chem. B* **2001**, *105*, 6474−6487.

(61) Kalé, L.; Skeel, P.; Bhandarkar, M.; R, B.; Gursoy, A.; Krawetz, N.; Philips, J.; Shinozaki, A.; Varadarajan, K.; Schulten, K. *J. Comput. Phys* **1999**, *151*, 283−312. http://www.ks.uiuc.edu/Research/namd/.

(62) Andersen, H. C. *J. Comput. Phys.* **1983**, *52*, 24−34.

(63) Essmann, U.; Perera, L.; L.Berkowitz, M.; Darden, T.; Lee, H.; Petersen, L. G. *J. Chem. Phys.* **1995**, *103*, 8577−8593.

(64) Feller, S. F.; Yuhong, Z.; Pastor, R. W. *J. Chem. Phys.* **1995**, *103*, 10267−10276.

ITT of a Biomimetic Elastin Model

J. Phys. Chem. B, Vol. 110, No. 8, 2006 **3587**

(65) Martyna, G. J.; Tobias, D. J.; Klein, M. L. *J. Chem. Phys.* **1994**, *101*, 4177−4189.

(66) Humphrey, W.; Dalke, A.; Schulten, K. *J. Mol. Graphics* **1996**, *14*, 33−38. http://www.ks.uiuc.edu/Research/vmd/.

(67) García, A. E. *Phys. Rev. Lett.* **1992**, *68*, 2696−2699.

(68) Amadei, A.; Linssen, A. B. M.; Berendsen, H. J. C. *Proteins: Struct., Funct., Genet.* **1993**, *17*, 412−425.

(69) Hyvärinen, A.; Karhunen, J.; Oja, E. *Independent Component Analysis*; John Wiley & Sons: New York, 2001; Chapter 6.

(70) Balsera, M. A.; Wriggers, W.; Oono, Y.; Schulten, K. *J. Phys. Chem.* **1996**, *100*, 2567−2572.

(71) Chandler, D. *Introduction to Modern Statistical Mechanics*; Oxford University Press: New York, 1987.

(72) Löffler, G.; Schreiber, H.; Steinhauser, O. *J. Mol. Biol.* **1997**, *270*, 520−534.

(73) Boresch, S.; Willensdorfer, M.; Steinhauser, O. *J. Chem. Phys.* **2004**, *120*, 3333−3347.

(74) Schultheis, V.; Hirschberger, T.; Carstens, H.; Tavan, P. *J. Chem. Theory Comput.* **2005**, *1*, 515−526.

(75) Flyvbjerg, H.; Petersen, H. G. *J. Chem. Phys.* **1989**, *91*, 461−466.

(76) Frenkel, D.; Smit, B. *Understanding Molecular Simulation: From Algorithms to Applications*; Academic Press: San Diego, CA, 2002; Appendix D.3.

(77) Yao, X. L.; Hong, M. *J. Am. Chem. Soc.* **2004**, *126*, 4199−4210.

(78) Additional material and visualizations on the topic of this paper can be found at http://www.theochem.rub.de/go/elastin.html.

(79) Lubchenko, V.; Wolynes, P. G.; Frauenfelder, H. *J. Phys. Chem. B* **2005**, *109*, 7488−7499.

(80) Despa, F.; Fernandez, A.; Berry, R. S. *Phys. Rev. Lett.* **2004**, *93*, 228104.

(81) Despa, F.; Fernandez, A.; Berry, R. S. *Phys. Rev. Lett.* **2004**, *93*, 269901.

(82) Höchtel, P.; Boresch, S.; Bitomsky, W.; Steinhauser, O. *J. Chem. Phys.* **1998**, *109*, 4927−4937.

(83) Smith, P. E.; van Gunsteren, W. F. *J. Chem. Phys.* **1994**, *100*, 3169−3174.

(84) Boresch, S.; Steinhauser, O. *Ber. Bunsen−Ges. Phys. Chem.* **1997**, *101*, 1019−1029.

(85) Rønne, C.; Thrane, L.; Åstrand, P.-O.; Wallqvist, A.; Mikkelsen, K. V.; Keiding, S. R. *J. Chem. Phys.* **1997**, *107*, 5319−5331.

(86) Okada, K.; Yao, M.; Kohno, Y.; Kajihara, Y. *J. Chem. Phys.* **1999**, *110*, 3026−3036.

(87) Buchner, R.; Barthel, J.; Stauber, J. *Chem. Phys. Lett.* **1999**, *306*, 57−63.

(88) Nabokov, O. A.; Lubimov, Y. A. *Mol. Phys.* **1988**, *65*, 1473−1482.

(89) Merrit, E. A.; Bacon, D. J. *Methods Enzymol.* **1997**, *277*, 505−524.

(90) Stone, J. An Efficient Library for Parallel Ray Tracing and Animation. Master's Thesis, Computer Science Department, University of Missouri−Rolla, 1998.